Geophys. J. Int. (2002) **151,** 924–934

Three-dimensional DC resistivity forward modelling using finite elements in comparison with finite-difference solutions

Yuguo Li* and Klaus Spitzer

Institut für Geophysik, TU Bergakademie Freiberg, Gustav-Zeuner-Straße 12, 09596 *Freiberg, Germany.*
E-mails: yli@geophysik.tu-freiberg.de; klaus.spitzer@geophysik.tu-freiberg.de

Accepted 2002 July 12. Received 2002 July 12; in original form 2001 November 26

SUMMARY

A 3-D finite-element scheme for direct current resistivity modelling is presented. The singularity is removed by formulating the problem in terms of the secondary potential, which improves the accuracy considerably. The resulting system of linear equations is solved using the conjugate gradient method. The incomplete Cholesky preconditioner with a scaled matrix has been proved to be faster than the symmetric successive overrelaxation preconditioner. A compact storage scheme fully utilizes the sparsity and symmetry of the system matrix.

The finite-element (FE) and a previously developed finite-difference (FD) scheme are compared in detail. Generally, both schemes show good agreement, the relative error in apparent resistivity for a vertical dike model presented in this paper is less than 0.5 per cent overall. The FD scheme produces larger errors near the conductivity contrast, whereas the FE scheme requires approximately 3.4 times as much storage as the FD scheme and is less robust with respect to coarse grids.

As an improvement to the forward modelling scheme, a modified singularity removal technique is presented. A horizontally layered earth or a vertical contact is regarded as the normal structure, the solution of which is the primary potential. The effect of this technique is demonstrated by two examples: a cube in two-layered earth and a cube near a vertical contact.

Key words: 3-D resistivity modelling, DC geoelectrics, finite differences, finite elements, preconditioning, singularity removal.

1 INTRODUCTION

A limited number of numerical solutions of the 3-D direct current (DC) resistivity problem have been discussed in the geophysical literature. These solutions have been obtained using integral equation, finite-difference or finite-element techniques. The integral equation method is most efficient for modelling one or a few inhomogeneous bodies in a homogeneous earth. Finite-difference (FD) and finite-element (FE) methods, however, are suitable for modelling an arbitrarily complex 3-D earth. Dey & Morrison (1979) developed a 3-D FD algorithm to evaluate the potential for a point current source. The equation of continuity is integrated over elemental volumes to obtain a system of self-adjoint difference equations. A mixed boundary condition was introduced, based on the asymptotic behaviour of the potential field in a homogeneous medium. Lowry *et al.* (1989) proposed a 3-D integrated FD scheme using a singularity removal technique. This method actually models the anomalous potential that is caused by conductivity contrasts. Spitzer (1995) reported a FD algorithm using conjugate gradient methods. A compact storage scheme was employed, which reduced the number of memory-resident coefficients and shortened the run time by avoiding unnecessary computational operations. Zhang *et al.* (1995) introduced a resistivity network formulation in conjunction with an inversion scheme. Two modifications of the FD method were recently made by Zhao & Yedlin (1996). The first is more accurate formulae for the source singularity removal. The second is the analytic computation of the source terms that arise from the decomposition of the potential into the primary and secondary potential. Spitzer *et al.* (1999) presented a secondary potential 3-D DC and induced polarization (IP) FD code, which offers grid-independent electrode positioning and detaches both transmitters and receivers from grid nodes. The application of the FE method to the 2-D resistivity problem was discussed by Coggon (1971). A FE solution to the 3-D resistivity problem was reported by Pridmore *et al.* (1981) and Xu (1994). Sasaki (1994) developed a 3-D resistivity inversion algorithm using the FE method. Recently, Zhou & Greenhalgh (2001) published a FE solution to the 3-D DC problem, where mixed boundary conditions and a compact storage scheme were incorporated. However, they solved the governing equation of the total potential.

In this paper, we revisited the 3-D FE resistivity forward problem, however, a modified method of singularity removal is presented to improve the stability of the solution. First, the theoretical basis of the FE solution for the secondary potential is developed. Furthermore,

*Now at: Fachrichlung Geophysik, Freie Universität Berlin, Berlin, Germany.

two different preconditioning methods, the incomplete Cholesky (IC) and the symmetric successive overrelaxation method (SSOR), are investigated. After that, the FE and FD schemes are compared in terms of accuracy and memory requirements. Finally, the effect of singularity removal is illustrated.

2 THE BOUNDARY VALUE PROBLEM

We assume a 3-D conductivity model $\sigma(x, y, z)$ in a Cartesian system of coordinates (x, y, z) with the origin at the air–earth interface and z positive downwards. The current source I is located at a point (x_q, y_q, z_q). The governing equation for the electrical potential $v(x, y, z)$ is

$$\nabla \cdot [\sigma(x, y, z)\nabla v(x, y, z)] = -I\delta(x - x_q)\delta(y - y_q)\delta(z - z_q), \tag{1}$$

where δ is the Dirac delta function.

Numerical approximations using eq. (1) typically give poor results in the vicinity of the source location because of steep gradients of the field. A better approach is to remove the effect of the singular potential caused by the source. According to the singularity removal procedure proposed by Lowry *et al.* (1989), the potential in eq. (1) is split into the primary potential v_n caused by the current source in a uniform half-space with the conductivity σ_n and the secondary potential v_a caused by the inhomogeneity with the anomalous conductivity $\sigma_a(x, y, z) = \sigma(x, y, z) - \sigma_n$, yielding

$$v(x, y, z) = v_n(x, y, z) + v_a(x, y, z). \tag{2}$$

The primary potential v_n satisfies the partial differential equation

$$\nabla \cdot [\sigma_n(x, y, z)\nabla v_n(x, y, z)] = -I\delta(x - x_q)\delta(y - y_q)\delta(z - z_q). \tag{3}$$

For a uniform half-space and a current source located at the surface of the earth, the solution of eq. (3) is

$$v_n = \frac{I}{2\pi\sigma_n r}, \tag{4}$$

where $r = \sqrt{(x - x_q)^2 + (y - y_q)^2 + z^2}$ is the distance from the measuring point to the source, while σ_n is the conductivity of the media at the source point (Zhao & Yedlin 1996).

With the above procedure, the singularity can be well removed and the discretization error in the vicinity of the source location becomes small. Especially when the background is a uniform half-space, the numerical results are of satisfactory accuracy over the whole model domain. However, if the background is a horizontally layered earth or a vertical contact, the numerical results can be distorted near the model domain boundaries. In this case, we make a refinement on the above described method. We assume that the primary potential is caused by the current source in a horizontally layered earth or in two quarter-spaces. The potential of a vertical contact can be calculated very easily using the method of images. Although a general expression for the potential at any point within a layered earth was given by Koefoed (1979) and Parasnis (1986), the recurrence formulae for all kernel functions, to our knowledge, are not available in the literature. Therefore, they are given in Appendix A.

Substituting eqs (2) and (3) into eq. (1), we obtain the differential equation for the secondary potential

$$\nabla \cdot [\sigma(x, y, z)\nabla v_a(x, y, z)] + \nabla \cdot [\sigma_a(x, y, z)\nabla v_n(x, y, z)] = 0. \tag{5}$$

To solve eq. (5), the boundary conditions must be defined. On boundaries with different conductivities, the total potential v and the normal component of the current density $j_n = \sigma\,\partial v/\partial n$ must be continuous, where **n** denotes the outward normal direction of the boundary interface. From this, we can further derive the continuity of the secondary potential v_a and $\sigma\,\partial v_a/\partial n + \sigma_a \partial v_n/\partial n$ on such boundaries. Since there is no current flow through the air–earth interface $\Gamma_s \in \Gamma$, where Γ denotes the boundary of the whole model domain, we have

$$\frac{\partial v_n}{\partial n} = 0, \quad \frac{\partial v_a}{\partial n} = 0 \quad \text{on } \Gamma_s. \tag{6}$$

On the outside domain boundaries $\Gamma_\infty \in \Gamma$, mixed boundary conditions (Dey & Morrison 1979) are applied:

$$\frac{\partial v_n}{\partial n} + \frac{\cos(r, n)}{r} v_n = 0, \quad \frac{\partial v_a}{\partial n} + \frac{\cos(r, n)}{r} v_a = 0, \tag{7}$$

where r denotes the radial distance from the source location to the boundary and **n** denotes the outward normal direction at the boundary surface.

For arbitrarily shaped 3-D structures, the above boundary value problem has to be solved numerically, e.g. by using the FE or FD method. In the following, we first formulate the FE solution. For a comparison with the FD method, we refer to the formulation given by Dey & Morrison (1979), Zhang *et al.* (1995), Spitzer (1995) and Spitzer & Wurmstich (1999).

3 FORMULATION OF THE FE EQUATIONS

The FE approximation of the governing eq. (5) is performed on a model volume that entirely embraces the volume of the 3-D inhomogeneities, and extends far enough in all directions for the anomalous potential to fade out to sufficient smallness on the outside boundary of the model volume. For most models, if the boundaries are far from the inhomogeneity, the secondary potential is mainly a dipole field and will go to zero at least as fast as $1/r^2$ (Zhao & Yedlin 1996). In this paper, we use the variational method to derive the FE equations. According to the variational principle, the true solution of a differential equation gives a stationary value to a functional. The functional can be formed by using the minimum theorem (Pridmore *et al.* 1981). For eq. (5), the functional reads

$$I(v_a) = \int_\Omega \left[\sigma(\nabla v_a)^2 + 2\sigma_a \nabla v_n \cdot \nabla v_a\right] d\Omega, \tag{8}$$

where Ω denotes the model volume. The variation of eq. (8) with respect to v_a yields

$$\delta I(v_a) = \int_\Omega 2(\sigma\nabla v_a + \sigma_a \nabla v_n) \cdot \nabla \delta v_a \, d\Omega. \tag{9}$$

Using the vector formulae

$$\nabla a \cdot \mathbf{b} = \nabla \cdot (a\mathbf{b}) - a\nabla \cdot \mathbf{b}, \tag{10}$$

and the divergence theorem

$$\int_\Omega \nabla \cdot \mathbf{b}\, d\Omega = \oint_\Gamma \mathbf{b} \cdot \mathbf{n}\, d\Gamma, \tag{11}$$

where a is an arbitrary scalar, **b** an arbitrary vector, $\Gamma = \Gamma_s + \Gamma_\infty$ represents the boundary surface of the model volume Ω and **n** is the outward normal direction of the boundary Γ, eq. (9) then becomes

$$\delta I(v_a) = 2\oint_{\Gamma_s + \Gamma_\infty} \left(\sigma \frac{\partial v_a}{\partial n} + \sigma_a \frac{\partial v_n}{\partial n}\right) \delta v_a \, d\Gamma - 2\int_\Omega [\nabla \cdot (\sigma\nabla v_a + \sigma_a \nabla v_n)]\delta v_a \, d\Omega. \tag{12}$$

The volume integral in eq. (12) is equal to zero, because the integrand is always zero according to eq. (5). From eq. (6), the surface integral at the air–earth interface Γ_s must also vanish. Thus, eq. (12) reduces to

$$\delta I(v_a) = 2\int_{\Gamma_\infty}\left(\sigma\frac{\partial v_a}{\partial n}+\sigma_a\frac{\partial v_n}{\partial n}\right)\delta v_a\, d\Gamma. \tag{13}$$

Insertion of eq. (7) into eq. (13) gives

$$\begin{aligned}\delta I(v_a) &= -2\int_{\Gamma_\infty}\left[\sigma\frac{\cos(r,n)}{r}v_a+\sigma_a\frac{\cos(r,n)}{r}v_n\right]\delta v_a\, d\Gamma\\ &= -\delta\int_{\Gamma_\infty}\left[\sigma\frac{\cos(r,n)}{r}v_a^2+2\sigma_a\frac{\cos(r,n)}{r}v_n v_a\right]d\Gamma,\end{aligned} \tag{14}$$

or

$$\delta\left\{I(v_a)+\int_{\Gamma_\infty}\left[\sigma\frac{\cos(r,n)}{r}v_a^2+2\sigma_a\frac{\cos(r,n)}{r}v_n v_a\right]d\Gamma\right\}=0. \tag{15}$$

In summary, the boundary value problem (5)–(7) is equivalent to the following variational problem:

$$\begin{aligned}F(v_a) &= \int_\Omega\left[\sigma(\nabla v_a)^2+2\sigma_a\nabla v_n\cdot\nabla v_a\right]d\Omega\\ &\quad+\int_{\Gamma_\infty}\left[\sigma\frac{\cos(r,n)}{r}v_a^2+2\sigma_a\frac{\cos(r,n)}{r}v_n v_a\right]d\Gamma,\\ \delta F(v_a) &= 0.\end{aligned} \tag{16}$$

The model volume Ω is subdivided into hexahedral elements, and the conductivity in each element is assumed to be constant. Then, the integral of eq. (16) is decomposed into integrals of each element, yielding

$$\begin{aligned}F(v_a) = &\sum_{e=1}^{n_e}\int_{\Omega_e}\sigma(\nabla v_a)^2\,d\Omega+\sum_{\Gamma_\infty}\int_{\Gamma_e}\sigma\frac{\cos(r,n)}{r}v_a^2\,d\Gamma\\ &+2\left[\sum_{e=1}^{n_e}\int_{\Omega_e}\sigma_a\nabla v_n\cdot\nabla v_a\,d\Omega\right.\\ &\left.+\sum_{\Gamma_\infty}\int_{\Gamma_e}\sigma_a\frac{\cos(r,n)}{r}v_n v_a\,d\Gamma\right],\end{aligned} \tag{17}$$

where Ω_e denotes the volume of a particular element e, Γ_e is the surface on Γ_∞ and n_e is the number of hexahedral elements.

We further assume that in each hexahedral element the primary and secondary potentials are linear functions of the Cartesian coordinates x, y and z, i.e.

$$v_n=\sum_{i=1}^{8}N_i v_{n,i},\quad v_a=\sum_{i=1}^{8}N_i v_{a,i}, \tag{18}$$

where $v_{n,i}$ and $v_{a,i}$ are the primary potential and the secondary potential, respectively, at the corner point i of a hexahedral element ($i=1,\ldots,8$) defined in global coordinates (see Fig. 1a), while N_i are linear shape functions defined by Xu (1994) and Li (2000) as

$$N_i=\frac{1}{8}(1+\xi_i\xi)(1+\eta_i\eta)(1+\zeta_i\zeta),\quad i=1,\ldots,8. \tag{19}$$

In eq. (19), ξ_i, η_i and ζ_i are the coordinates of the corner point i in the local coordinates (ξ, η, ζ) (see Fig. 1b).

A major step in the FE method is to transform the global coordinates (x, y, z) into corresponding local coordinates (ξ, η, ζ) by

$$\xi=\frac{2}{a}(x-x_c),\quad \eta=\frac{2}{b}(y-y_c),\quad \zeta=\frac{2}{c}(z-z_c), \tag{20}$$

where x_c, y_c and z_c are the coordinates of the centre of the hexahedral element, a, b and c are the length, width and height of the hexahedral element, respectively. This transformation simplifies the evaluation of the integrals in eq. (17). Using eqs (18)–(20), the volume integrals in eq. (17) are analytically evaluated in the local coordinates.

Similarly, the surface integrals in eq. (17) are evaluated analytically. In this case, the potentials v_n and v_a are determined by linear interpolation of the potentials at four nodes of a rectangular element.

Summing up the integrals over all elements and assembling the element matrices to a system matrix, we obtain the following approximation to the functional $F(v_a)$:

$$F(v_a)=\mathbf{v}_a^{\mathrm{T}}\mathbf{K}\mathbf{v}_a+2\mathbf{v}_a^{\mathrm{T}}\mathbf{p}, \tag{21}$$

where $\mathbf{K}$ is the total system matrix, $\mathbf{v}_a$ is the vector of the unknown secondary potentials at all nodes and $\mathbf{p}$ is the known vector resulting from the final two terms of the right-hand side of eq. (17). The superscript T denotes matrix transposition.

From eq. (21), the first variation of the functional F with respect to $\mathbf{v}_a$ is

$$\delta F(v_a)=2\delta\mathbf{v}_a^{\mathrm{T}}\mathbf{K}\mathbf{v}_a+2\delta\mathbf{v}_a^{\mathrm{T}}\mathbf{p}. \tag{22}$$

The functional is minimized by setting the first variation of the functional to zero. This finally results in the finite-element equation

$$\mathbf{K}\mathbf{v}_a=-\mathbf{p}, \tag{23}$$

where the system matrix $\mathbf{K}$ is symmetric and sparsely occupied by non-zero elements. This system of linear equations is solved numerically by using the conjugate gradient method (Hestenes & Stiefel 1952), which provides the anomalous potential at all nodal

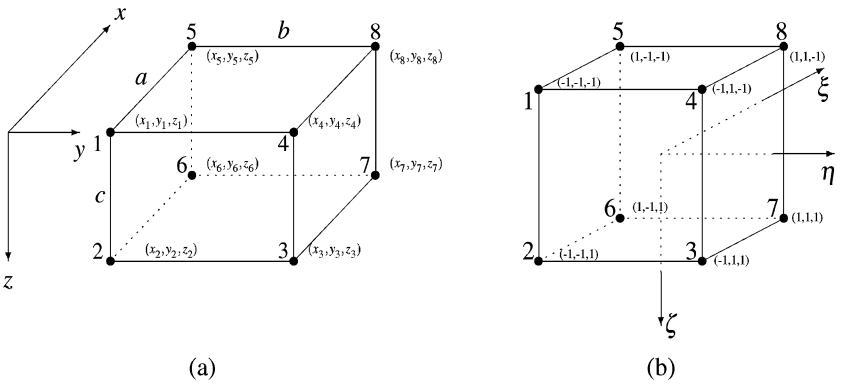

Figure 1. A hexahedral element in the global coordinate system (a) and in the local coordinate system (b) for FE modelling.

points. The total potential is then obtained by adding the anomalous potential to the normal potential.

4 PRECONDITIONING

To solve the equation system efficiently by using the conjugate gradient method, it is often conventional to apply a preconditioning technique. This decreases the condition number of the matrix and accelerates the convergence. Following the idea of preconditioning, the system of linear eq. (23) is transformed into an equivalent system

$$\mathbf{H}^{-1}\mathbf{K}\mathbf{v}_a = -\mathbf{H}^{-1}\mathbf{p}, \tag{24}$$

where $\mathbf{H}^{-1}$ is an approximate inverse of $\mathbf{K}$ with $\mathbf{H}^{-1}\mathbf{K} \approx \mathbf{I}$. Note that the identity matrix $\mathbf{I}$ has the condition number 1.

In the previous two decades, different methods for the choice of the preconditioning matrix $\mathbf{H}$ have been developed (Meijerink & van der Vorst 1977; Kershaw 1978; Manteuffel 1979; Axelsson 1985; Schwarz 1991). In the following, we investigate the efficiency of three preconditioning methods for solving our problem.

4.1 Scaling the coefficient matrix

Scaling the coefficient matrix is the simplest way of preconditioning. According to Schwarz (1991), the equation system (23) is written as

$$\tilde{\mathbf{K}}\tilde{\mathbf{v}}_a = -\tilde{\mathbf{p}}, \tag{25}$$

with

$$\tilde{\mathbf{K}} = \mathbf{D}\mathbf{K}\mathbf{D}, \quad \tilde{\mathbf{v}}_a = \mathbf{D}^{-1}\mathbf{v}_a, \quad \tilde{\mathbf{p}} = \mathbf{D}\mathbf{p},$$

where $D_{ij} = 0$ for $i \neq j$ and $D_{ij} = 1/\sqrt{K_{ij}}$ for $i = j$. The modified matrix $\tilde{\mathbf{K}}$ is still symmetric and maintains the non-zero pattern of $\mathbf{K}$. All diagonal elements of $\tilde{\mathbf{K}}$ are equal to 1. In general, scaling already decreases the condition number considerably.

4.2 SSOR preconditioning with a scaled matrix

Schwarz (1991) suggested the symmetric successive overrelaxation method. Following this method, the scaled coefficient matrix $\tilde{\mathbf{K}}$ in eq. (25) is presented by the sum of an identity matrix $\mathbf{I}$, a lower triangular matrix $\mathbf{E}$ and its transposition matrix $\mathbf{F} = \mathbf{E}^{\mathrm{T}}$ as

$$\tilde{\mathbf{K}} = \mathbf{E} + \mathbf{I} + \mathbf{F}. \tag{26}$$

The preconditioning matrix $\mathbf{H}$ is defined by

$$\mathbf{H} = \mathbf{C}\mathbf{C}^{\mathrm{T}} = (\mathbf{I} + \omega\mathbf{E})(\mathbf{I} + \omega\mathbf{F}), \tag{27}$$

where $\mathbf{C} = \mathbf{I} + \omega\mathbf{E}$. The matrix $\mathbf{C}$ is similar to the above defined matrix $\mathbf{E}$ and has the same non-zero pattern as the lower part of $\tilde{\mathbf{K}}$. In eq. (27), $\omega \in \mathbb{R}$ denotes a relaxation factor, which is chosen to be 1.4 for all our model tests. The SSOR preconditioner has the advantage of not requiring any additional memory because the preconditioning matrix is implicitly constructed and stored.

4.3 IC preconditioning with a scaled matrix

An alternative method for producing a preconditioning matrix $\mathbf{H}$ is based on an incomplete Cholesky decomposition of $\tilde{\mathbf{K}}$. In general, the IC decomposition fails, because the square roots of negative numbers may arise. Such a breakdown can occur even for the problem where $\tilde{\mathbf{K}}$ is symmetric and positive-definite. In this case, we use a correction scheme suggested by Manteuffel (1979) and Schwarz (1991), where the off-diagonal elements of the scaled matrix $\tilde{\mathbf{K}}$ in eq. (26) are reduced to

$$\tilde{\mathbf{K}}' = \mathbf{I} + \frac{1}{1+\alpha}(\mathbf{E} + \mathbf{F}) \tag{28}$$

with a small non-negative number α, which should be chosen to be as small as possible. The larger α is, the more strongly the absolute values of the off-diagonal elements of $\tilde{\mathbf{K}}$ are reduced, and then the matrix $\tilde{\mathbf{K}}'$ becomes increasingly a worse approximation to $\tilde{\mathbf{K}}$ and the preconditioning effect may be reduced. The suitable value of α is found by experiments. It is chosen to be $\alpha = 0.01$ for all model tests in this paper.

The preconditioning matrix $\mathbf{H}$ is defined by

$$\mathbf{H} = \mathbf{C}\mathbf{C}^{\mathrm{T}}, \tag{29}$$

where $\mathbf{C}$ is a lower triangular matrix, which describes an IC decomposition of the matrix $\tilde{\mathbf{K}}'$. The elements of $\mathbf{C}$ are determined recursively by

$$C_{ii} = \left(\tilde{K}'_{ii} - \sum_{l=1}^{i-1} C_{il}^2\right)^{1/2}, \tag{30}$$

$$C_{ji} = \left(\tilde{K}'_{ji} - \sum_{l=1}^{i-1} C_{jl}C_{il}\right) \Big/ C_{ii}, \quad \text{if } \tilde{K}'_{ji} \neq 0, \tag{31}$$

$$C_{ji} = 0, \quad \text{if } \tilde{K}'_{ji} = 0, \qquad i = 1, \ldots, n; \quad j = i+1, \ldots, n. \tag{32}$$

The matrix $\mathbf{C}$ has the same sparsity pattern as $\tilde{\mathbf{K}}'$. The IC preconditioner requires additional storage for the matrix $\mathbf{C}$.

A test was performed on a vertical dike model (Fig. 2). The dike is 5 m wide and 20 m offset from the origin of the coordinate system. It extends to infinity in $\pm x$- and $+z$-direction. The resistivity of the half-space and the dike are $\rho_1 = 100\ \Omega$ m and $\rho_2 = 10\ \Omega$ m, respectively. Schlumberger soundings are carried out over the structure. The two current sources are located at (0, −1, 0 m) and (0, 1, 0 m), respectively. The modelling domain boundaries are located at ±5500 m in the x- and y-directions and 5500 m in the $+z$-direction. The model is divided into 215 424 irregular cells using $73 \times 89 \times 35$ grid lines, yielding a total of 227 395 field unknowns. The system of equations is solved using the preconditioned conjugate gradient method. We use $\mathbf{v}_a^{(0)} = 0$ as starting values. In Fig. 3, the relative

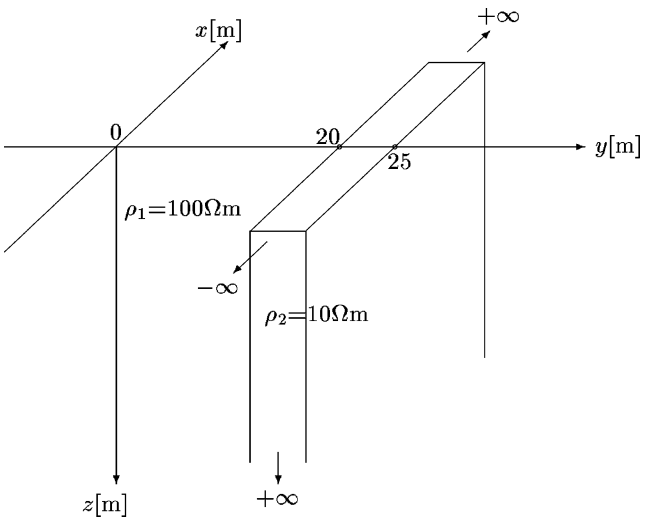

Figure 2. A vertical dike model.

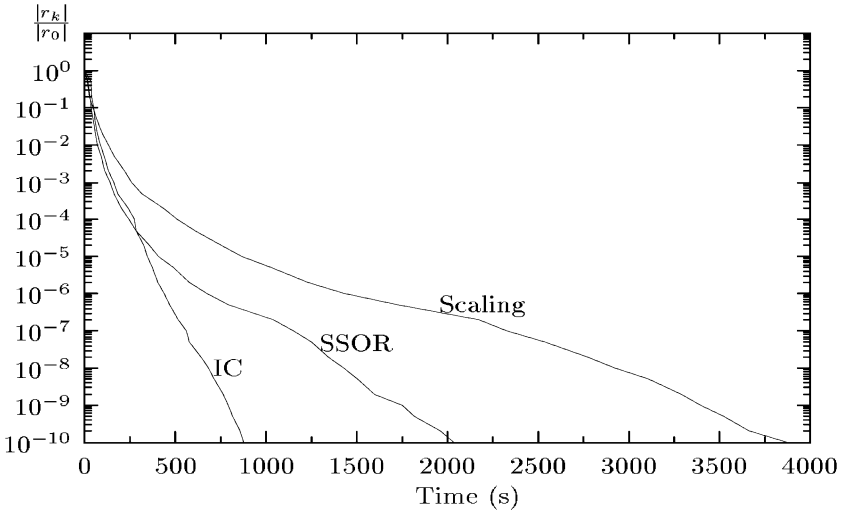

Figure 3. Convergence of three preconditioners for the vertical dike model in Fig. 2. The ordinate shows the norm of the residual of the kth iteration step $|\mathbf{r}_k|$ normalized by the residual of the first iteration step $|\mathbf{r}_0|$, and the abscissa shows the CPU time on the IBM RS/6000 computer.

norm of the residual $|\mathbf{r}_k|/|\mathbf{r}_0|$ is plotted versus the CPU time on the workstation IBM RS/6000 for all three preconditioning methods. $|\mathbf{r}_k| = \|-\tilde{\mathbf{p}} - \tilde{\mathbf{K}}\mathbf{v}_a^{(k)}\|$ is the residual of the kth iteration and $|\mathbf{r}_0| = \|-\tilde{\mathbf{p}} - \tilde{\mathbf{K}}\mathbf{v}_a^{(0)}\|$ is the residual of the first iteration. One sees that the IC method has the best convergence rate followed by SSOR and scaling. This implies that the SSOR method is a suitable choice for large 3-D grids, while the IC method is a good choice if sufficient computer memory is available.

5 COMPARISONS OF THE FE AND FD SCHEMES

The FE and FD technique tackle the boundary value problem using very different principles. Whereas the FD formulation directly transfers partial differential equations into difference equations, the FE method is based on the variational principle or the method of weighted residuals. In this section, we compare the FE method presented in this paper with the FD method given by Spitzer (1995) and Spitzer *et al.* (1999), in terms of accuracy and memory requirements to find the most effective approach to solving our 3-D modelling problem in the DC method.

5.1 Accuracy

The accuracies of the FE and FD schemes are compared for the previously described dike model (Fig. 2). All comparisons are carried out for a pole–pole configuration. A single current source is assumed to be located at the origin of the coordinate system.

An irregular grid with $61 \times 61 \times 31$ nodes is used for the FE and FD modelling. The model boundaries are at a distance of 5500 m in each direction. The model is more finely discretized near the conductivity contrast. In Fig. 4(a), the apparent resistivity ρ_a computed by both FE and FD algorithms is plotted versus the electrode distance of the pole–pole configuration. The profile extends parallel to the dike and along the $+x$-axis (i.e. $x > 0$ and $y = 0$). The solution computed by an analytical dike program (Hanstein 1994, pers. comm.) is also shown for comparison. It is seen that both FE and FD methods provide very accurate results over the whole range. The relative deviation between the numerical results and the analytical solution is less than 0.2 per cent (see Fig. 4b), except at the boundary ($x = 5500$ m), where the error reaches 1.15 per cent for the FE solution. This is probably caused by the conductive dike extending to the model boundary. The elongated elements along with improper boundary conditions produce poor results.

Fig. 5(a) shows the apparent resistivity ρ_a obtained by the FE and FD method for the pole–pole configuration together with analytical solution. The profile extends perpendicular to the dike and along the $+y$-axis (i.e. $x = 0$ and $y > 0$). The FE and FD solutions agree very well with the analytical results. However, the signature of the error distribution is different for each method (see Fig. 5b). Maximum errors between 0.20 and 0.54 per cent occur at $y = 20$–90 m for the FD solution, whereas for the FE solution the maximum errors occur between $y = 32.5$–200 m. If the model discretization is refined at $y = 10$–425 m, the accuracy of the FE scheme is improved considerably, yielding a relative error of less than 0.14 per cent over the whole range (Fig. 6). However, the maximum of the error for the FD scheme remains, although the amplitude is reduced. These model tests show that the FD scheme seems to be rather robust with respect to coarse grids, i.e. geometric grid properties, and the FE scheme with respect to conductivity contrasts. These differences are probably related to the treatment of potential and conductivity in assembling the coefficient matrix. A second-order Taylor series expansion of the potential is used for deriving the FD expressions (Spitzer 1995), but in assembling the FE matrix $\mathbf{K}$ it is assumed that the potentials are linear function of the coordinates in each hexahedral element. Thus, a local refinement of the grid in those regions where the potential fields vary steeply is more essential for FE than it is for FD to obtain accurate results. Moreover, in assembling FE coefficients the electrical conductivity is assumed to be constant over each hexahedron and is equal to the real conductivity of the medium. However, in the FD scheme the conductivity value at a grid point is the arithmetic average of eight volume-weighted cell conductivities that surround the grid point (Spitzer 1995). This approximation accounts for increased discretization errors near the conductivity contrast. Uncontrollable numerical instabilities of the FD solution are therefore observed in the case of a very high conductivity contrast. Fig. 7 shows the FE and FD results of a pole–pole configuration for the conductivity contrast of $\rho_1/\rho_2 = 10\,000$ (i.e. $\rho_1 = 100\ \Omega$ m and $\rho_2 = 0.01\ \Omega$ m). The FE solution agrees well with

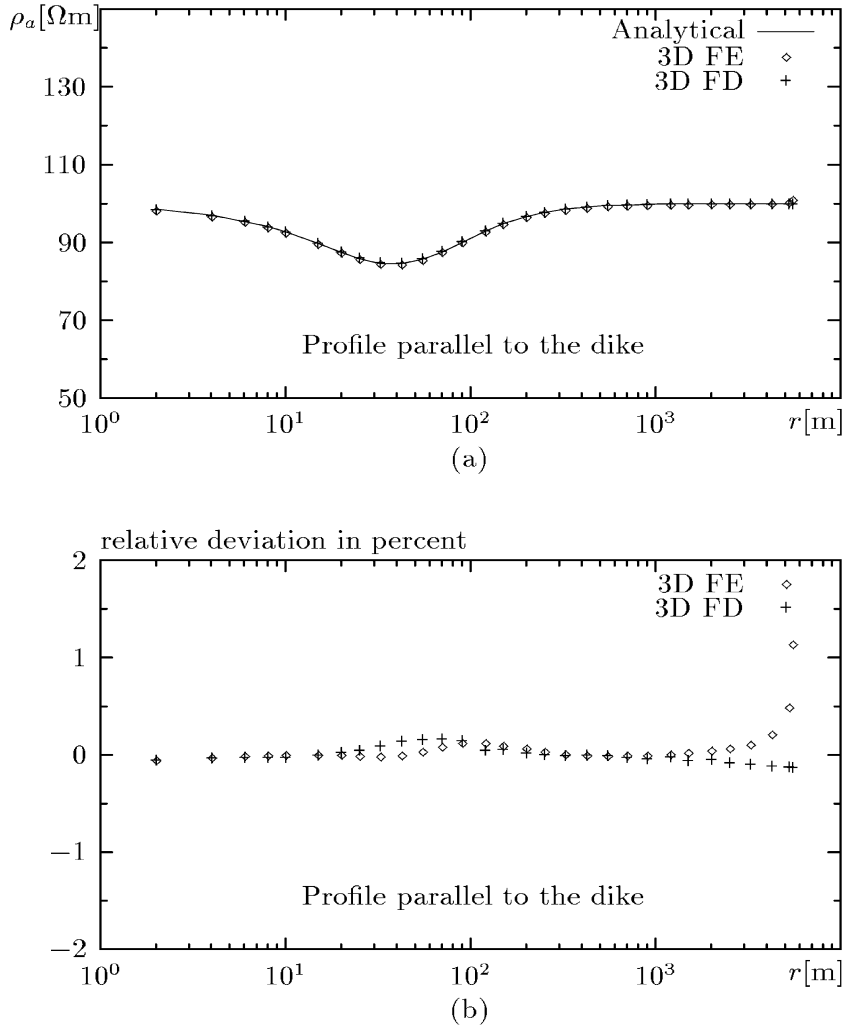

Figure 4. Comparison of the DC apparent resistivity obtained from FE and FD (top) and the relative deviation between the numerical result and the analytical solution (bottom) versus the electrode distance for a pole–pole configuration along the $+x$-axis parallel to the dike in Fig. 2.

the analytical one after refining the grid adequately. However, it is not possible to restabilize the FD solution.

5.2 Storage size of coefficient matrix

As mentioned in Section 3, the coefficient matrix of the FE equations is symmetric and sparse. With the hexahedral-element discretization, each node has a maximum of 26 neighbouring nodal points. This means that the coefficient matrix generally has 27 non-zero elements in each row. Owing to the symmetry of the matrix, 14 non-zero elements need to be stored in each row. For a grid with, for example, $73 \times 89 \times 35$ nodes, there are $\sim 3.1 \times 10^6$ non-zero elements to be stored.

Most 3-D FD approaches are formulated with a central grid point and its six direct neighbours along the main coordinate axes. This means that the coefficient matrix resulting from FD discretization has a maximum of seven non-zero elements in each row. Considering the symmetry, there are only four non-zero elements to be stored in each row. For the above grid of $73 \times 89 \times 35$, there are $\sim 9.1 \times 10^5$ non-zero elements to be stored.

From the above discussion, we conclude that the FD method has a much smaller storage requirement than the FE method. For our example of a grid with $73 \times 89 \times 35$ nodes, the FE scheme requires approximately 3.4 times as much storage as the FD scheme.

6 IMPROVED SINGULARITY REMOVAL TECHNIQUE

In this section, we first show the superiority of the singularity removal technique and then illustrate the advantages of using more suitable reference models for the potential split-up. So far, the homogeneous half-space has been most frequently used to calculate the normal potential (Lowry *et al.* 1989; Xu 1994; Zhao & Yedlin 1996). However, for a wide range of models, horizontal layers or vertical contacts are better alternatives. We refer to the former method as the conventional singularity removal technique and the latter as the improved singularity removal technique. In the following, the vertical dike model given in Fig. 2 is studied to show the advantage of modelling the secondary potential, whereas a cube buried in a two-layered earth, and a cube buried near a vertical fault are considered to demonstrate the superiority of the improved singularity removal technique.

Fig. 8(a) shows the apparent resistivity ρ_a of a Schlumberger configuration for a profile along the y-axis perpendicular to the dike.

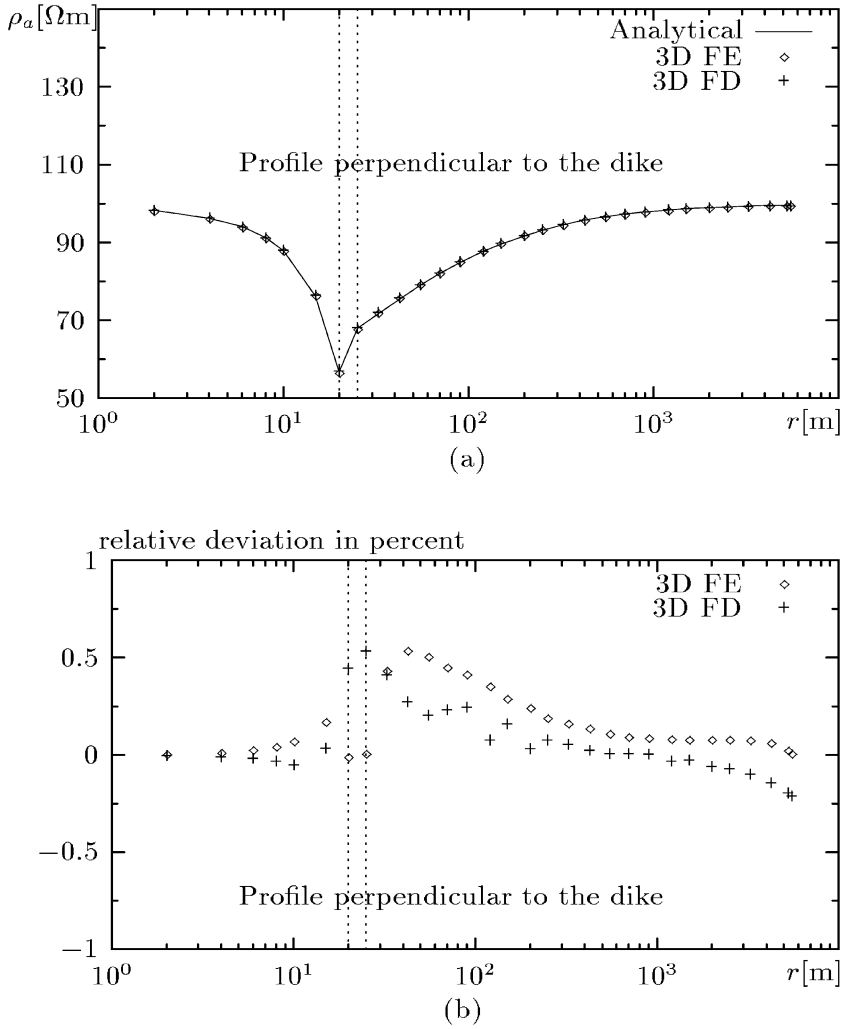

Figure 5. Comparison of the DC apparent resistivity obtained from FE and FD (top) and the relative deviation between the numerical result and the analytical solution (bottom) versus the electrode distance for a coarse grid and a pole–pole configuration along the $+y$-axis perpendicular to the dike in Fig. 2. The dotted lines indicate the dike boundaries. The signature of the error distribution is different for the FE and FD method.

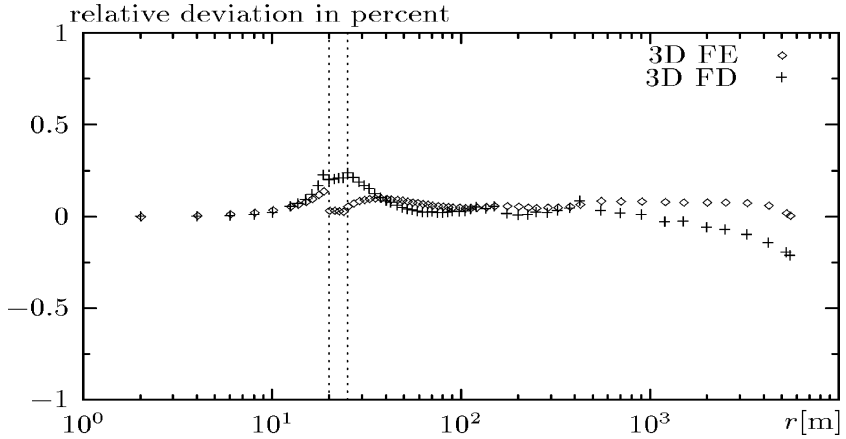

Figure 6. Relative deviation between the numerical results and the analytical solution for a fine grid and the dike model in Fig. 2. The electrode array is the same as that used in Fig. 5. The dotted lines indicate the dike boundaries. Refinement of the grid mainly reduces the error for FE.

The two current sources are located at $(0, -1, 0\,\text{m})$ and $(0, 1, 0\,\text{m})$, respectively. The apparent resistivity ρ_a is obtained by directly solving the differential eq. (1). The results from the conventional singularity removal technique are also presented. It is clear from Fig. 8 that the method without singularity removal produces larger errors than the method with the conventional singularity removal, especially near the current source point. The average error, which is calculated as the sum of the percentage error at all profile nodes divided by the

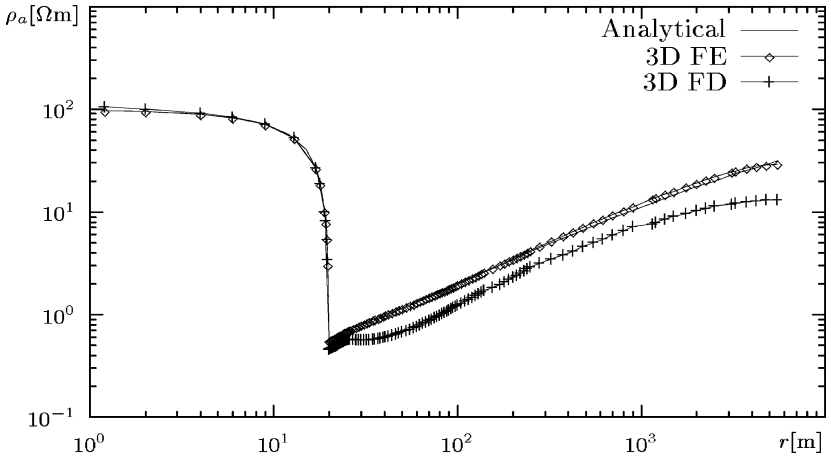

Figure 7. DC apparent resistivity versus the electrode distance for a pole–pole configuration and a large conductivity contrast of $\rho_1/\rho_2 = 10^4$ ($\rho_1 = 100$ and $\rho_2 = 0.01$ Ω m) for the dike model in Fig. 2. After refining the grid, the FE solution becomes more accurate, whereas the FD solution remains unstable.

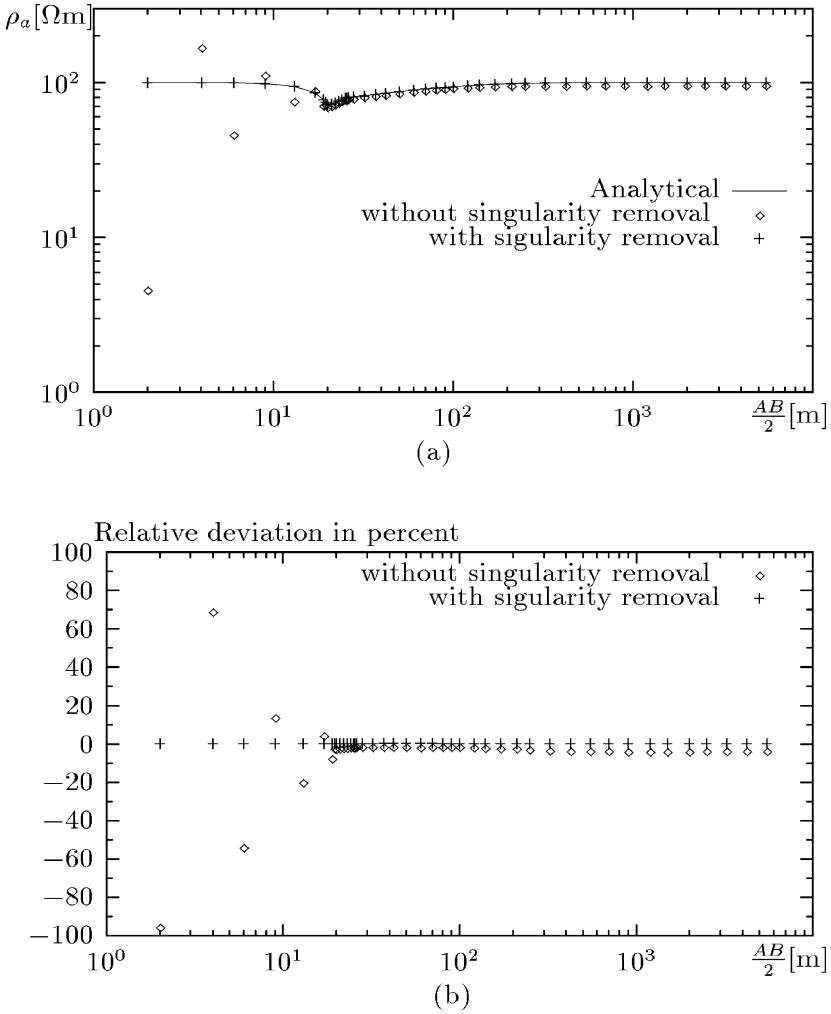

Figure 8. The effect of singularity removal for a Schlumberger configuration along the y-axis perpendicular to the dike depicted in Fig. 2. Part (a) shows the apparent resistivity ρ_a versus half of the electrode distance of the Schlumberger sounding (AB/2); (b) the relative deviation between the FE result and the analytical solution. Note the small errors near the source for the singularity removal technique.

number of nodes, is 8.02 per cent for the FE solution without singularity removal and 0.13 per cent for the FE solution with singularity removal. This example demonstrates that a secondary potential approach improves the accuracy considerably.

The second model is a cube buried in a two-layered earth shown in Fig. 9(a). The first layer has a resistivity of $\rho_1 = 100$ Ω m and a thickness of $h = 3$ m. The underlying half-space has a resistivity of $\rho_2 = 10$ Ω m. A conducting cube with a resistivity of $\rho_3 = 10$ Ω m

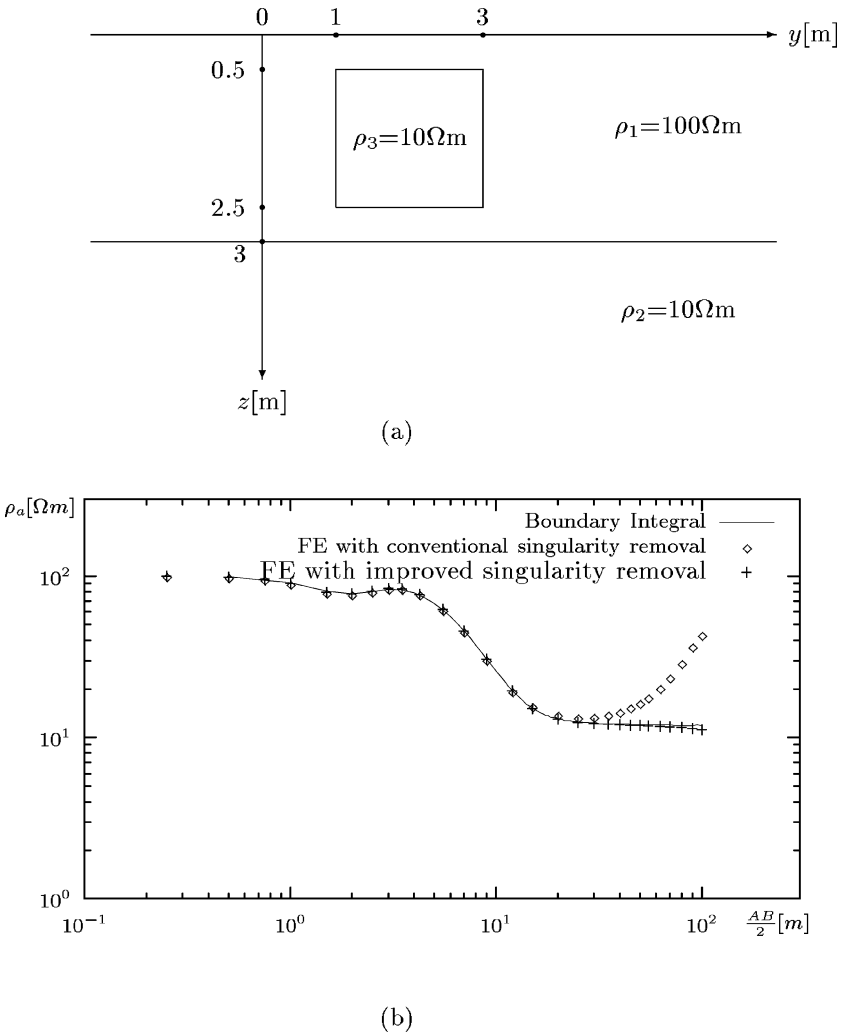

Figure 9. The effect of singularity removal for a Schlumberger sounding, where two current sources are located at (0, −0.1, 0 m) and (0, 0.1, 0 m), respectively. Part (a) shows a cube model buried in a two-layered earth and (b) the DC apparent resistivity ρ_a versus half of the electrode distance of a Schlumberger sounding (AB/2). The improved singularity removal technique increases the accuracy toward the boundaries significantly.

and side length of 2 m is embedded in the first layer. A Schlumberger sounding is carried out along the *y*-axis and the two current sources are located at (0, −0.1, 0 m) and (0, 0.1, 0 m). The apparent resistivity ρ_a is calculated using the FE method with the conventional and the improved singularity removal technique. For the latter, the two-layered earth ($\rho_1 = 100\ \Omega$ m, $h = 3$ m and $\rho_2 = 10\ \Omega$ m) is regarded as the normal structure. In Fig. 9(b), the apparent resistivity ρ_a is plotted versus half of the electrode distance of the Schlumberger configuration ($AB/2$). For comparison, the numerical result from a boundary-integral method (Hvoždara 1995) is also shown. It can be seen that the FE solution using the improved singularity removal technique agrees very well with the boundary-integral solution, whereas the FE solution using the conventional singularity removal technique shows huge deviations for large electrode spacings ($AB/2 > 15$ m). This example shows that the use of the conventional singularity removal technique with a homogeneous half-space as a reference model is inadequate when the background is a layered earth.

The same comparison is carried out for a cube buried near a vertical fault shown in Fig. 10(a). The current sources for a Schlumberger sounding are located at (0, −3.4, 0 m) and (0, −2.6, 0 m). The FE method with the improved singularity removal technique uses a vertical contact as the normal structure. In Fig. 10(b), the calculation results from the improved and conventional methods are compared again with those from a boundary-integral method (Hvoždara & Kaikkonen 1994). The improved singularity removal technique produces a small error of 3.1 per cent at the boundary, the numerical results obtained with the conventional singularity removal technique are distorted seriously.

7 CONCLUSIONS

In this paper, we have developed a 3-D finite-element algorithm for DC resistivity modelling with incorporation of the singularity removal technique and mixed boundary conditions. We have demonstrated that with the conventional singularity removal technique, when the background structure is a uniform half-space, the singularity can be removed in the vicinity of the current source and the numerical results are of higher accuracy over the whole model domain. However, if the background is not a homogeneous half-space, this technique may fail. To solve this problem, we have introduced

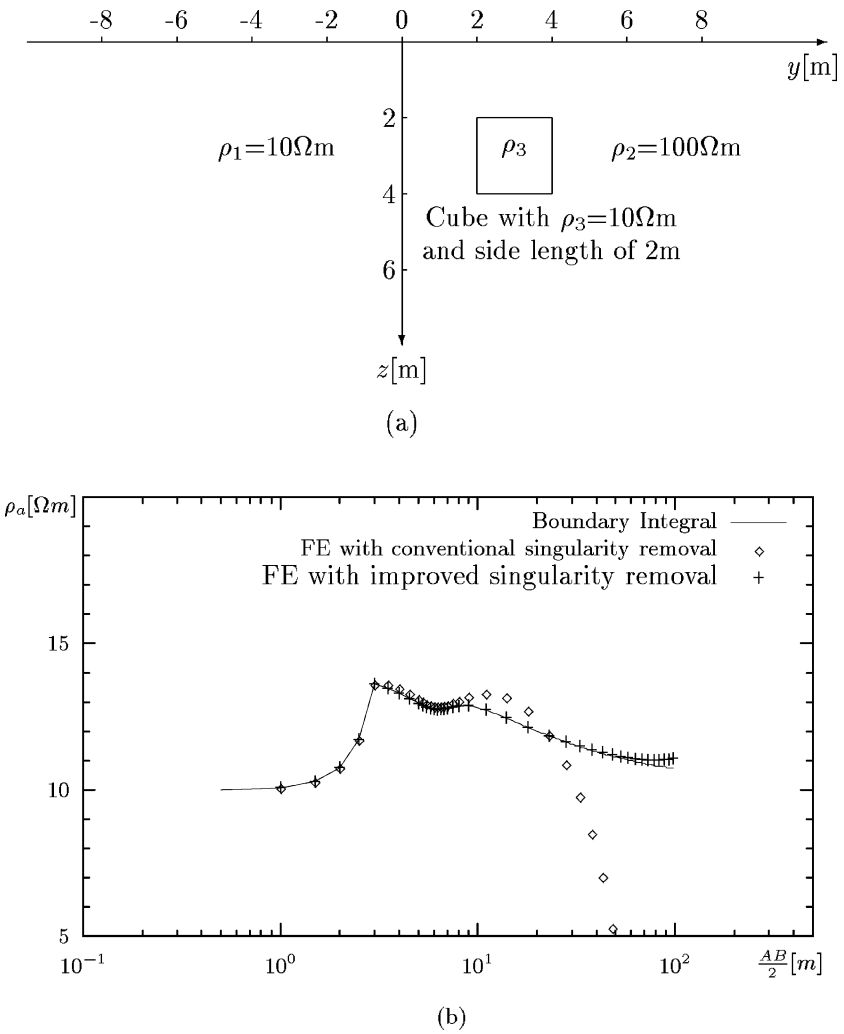

Figure 10. The effect of singularity removal for a Schlumberger sounding, where two current sources are located at (0, −3.4, 0 m) and (0, −2.6, 0 m), respectively. Part (a) shows a cube model buried near a vertical contact and (b) the DC apparent resistivity ρ_a versus half of the electrode distance of a Schlumberger sounding (AB/2). The improved singularity removal technique is again superior to the conventional one.

an improved singularity removal technique, where the solution of a horizontally layered earth or a vertical contact is regarded as the primary potential. This technique works well for a wide range of models and increases the accuracy considerably toward the boundaries.

Our studies have shown that the preconditioned conjugate gradient method is a very effective solver for 3-D finite-element equations. The SSOR preconditioner provides a fast convergence rate without additional memory requirements. IC decomposition with a scaled matrix is even faster, but at the expense of increased memory allocation.

From the numerical tests presented in this paper we conclude that both FE and FD methods give accurate results when an appropriate grid is used. In comparison with the FE method, the FD method requires less storage, but it produces larger errors near conductivity contrasts. On the other hand, the FE method produces smaller errors near conductivity contrast, but it requires more storage and is less robust with respect to coarser grids. In this paper, we have used hexahedral elements for FE modelling, so that the results are comparable with those from the FD method. Our future aim is the incorporation of tetrahedral grids for a better handling of complicated topography and sloping interfaces.

ACKNOWLEDGMENTS

This work is financially supported by the Deutsche Forschungsgemeinschaft (Ja 590/18-1). Part of the calculations have been performed at the Geophysical Institute of the University of Göttingen. Our thanks go to Professor U. Christensen for providing the necessary facilities. We also wish to thank T. Hanstein and M. Hvoždara for providing an analytical dike program and a boundary integral code. We would like to thank Ashok Agarwal and an anonymous reviewer for critical reviews and comments.

REFERENCES

Axelsson, O., 1985. A survey of preconditioned iterative methods for linear systems of equations, *BIT,* **25,** 166–178.

Coggon, J.H., 1971. Electromagnetic and electrical modeling by the finite element method, *Geophysics,* **36,** 132–155.

Dey, A. & Morrison, H.F., 1979. Resistivity modeling for arbitrarily shaped three-dimensional structures, *Geophysics,* **44,** 615–632.

Hestenes, M.R. & Stiefel, E., 1952. Method of conjugate gradients for solving linear systems, *J. Res. Nat. Bur. Standards,* **49,** 409–436.

Hvoždara, M., 1995. The boundary integral calculation of the DC geoelectric field due to a point current source on the surface of 2-layered earth with

a 3-D perturbing body buried or outcropping, *Contr. Geophys. Inst. Slov. Acad. Sci.,* **25,** 7–24.

Hvoždara, M. & Kaikkonen, P., 1994. The boundary integral calculations of the forward problem for DC sounding and MMR methods for a 3-D body near a vertical contact, *Studia geoph. geod.,* **38,** 375–398.

Kershaw, D., 1978. The incomplete Cholesky-conjugate gradient method for the iterative solution of systems of linear equations, *J. Comp. Phys.,* **26,** 43–65.

Koefoed, O., 1979. *Geosounding Principles,* Vol. 1, Elsevier, Amsterdam.

Li, Y., 2000. Finite element modeling of electromagnetic fields in two- and three-dimensional anisotropic conductivity structures, *PhD thesis,* Univ. Göttingen (in German).

Lowry, T., Allen, M.B. & Shive, P.N., 1989. Singularity removal: a refinement of resistivity modeling techniques, *Geophysics,* **54,** 766–774.

Manteuffel, T.A., 1979. Shifted incomplete Cholesky-factorization, in *Sparse Matrix Proceedings 1978,* eds Duff, I.S. & Stewart, G.W., SIAM, Philadelphia, PA.

Meijerink, J.A. & van der Vorst, H.A., 1977. An iterative solution method for linear systems of which the coefficient matrix is a symmetric *M*-matrix, *Math. Comp.,* **31,** 148–162.

Parasnis, D.S., 1986. *Principles of Applied Geophysics,* Chapman and Hall, London.

Pridmore, D., Hohmann, G.W., Ward, S.H. & Sill, W.R., 1981. An investigation of finite element modeling for electrical and electromagnetic modeling data in three dimensions, *Geophysics,* **46,** 1009–1024.

Sasaki, Y., 1994. 3-D resistivity inversion using the finite element method, *Geophysics,* **59,** 1839–1848.

Schwarz, H.R., 1991. *Methode der finiten Elemente: eine Einführung unter besonderer Berücksichtigung der Rechenpraxis,* Teubner, Stuttgart.

Spitzer, K., 1995. A 3-D finite-difference algorithm for DC resistivity modeling using conjugate gradient methods, *Geophys. J. Int.* **123,** 903–914.

Spitzer, K. & Wurmstich, B., 1999. Speed and accuracy in 3D resistivity modeling, in *Three-dimensional Electromagnetics,* Vol. 7, pp. 161–176, eds Oristaglio, M.L. & Spies, B.R., SEG Book Series, Geophysical Developments, Society of Exploration Geophysicists.

Spitzer, K., Chouteau, M. & Boulanger, O., 1999. Grid-independent electrode positioning for 3D DC resistivity and IP forward modeling, Extended Abstracts Book, 2nd Int. Symp. on Three-Dimensional Electromagnetics, University of Utah, Salt Lake City, UT, pp. 189–192.

Xu, S.Z., 1994. *Finite Element Method in Geophysics,* Science Press, Beijing (in Chinese).

Zhang, T., Mackie, R.L. & Madden, T.R., 1995. 3D resistivity forward modeling and inversion using conjugate gradients, *Geophysics,* **60,** 1313–1325.

Zhao, S. & Yedlin, M., 1996. Some refinements on the finite-difference method for 3-D dc resistivity modeling, *Geophysics,* **61,** 1301–1307.

Zhou, B. & Greenhalgh, S.A., 2001. Finite element three-dimensional direct current resistivity modeling: accuracy and efficiency considerations, *Geophys. J. Int.* **145,** 679–688.

APPENDIX A: RECURRENCE FORMULAE FOR KERNEL FUNCTIONS TO CALCULATE THE POTENTIAL AT ANY POINT IN A LAYERED EARTH

Consider an n-layer earth with thicknesses h_j and resistivities ρ_j ($j = 1, \ldots, n$). Let H_j be the depth of the bottom of the jth layer and assume the nth layer to extend to infinity, i.e. $h_n = \infty$ and $H_n = \infty$. The coordinate system (r, ϕ, z) is cylindrical with the current electrode as the origin and z positive downward.

Following Koefoed (1979) and Parasnis (1986), the potentials in the first layer and in the substratum read

$$v_1(r,z) = \frac{I\rho_1}{2\pi r}\int_0^\infty \mathrm{e}^{-\lambda z} J_0(\lambda r)\, d\lambda + \int_0^\infty A_1(\lambda)[\mathrm{e}^{-\lambda z} + \mathrm{e}^{\lambda z}] J_0(\lambda r)\, d\lambda \tag{A1}$$

$$v_n(r,z) = \int_0^\infty A_n(\lambda)\mathrm{e}^{-\lambda z} J_0(\lambda r)\, d\lambda \tag{A2}$$

and the potential in any layer j ($j \neq 1$, or n) is

$$v_j(r,z) = \int_0^\infty \left[A_j(\lambda)\mathrm{e}^{-\lambda z} + B_j(\lambda)\mathrm{e}^{\lambda z}\right] J_0(\lambda r)\, d\lambda, \tag{A3}$$

where J_0 is the Bessel function of the first kind of order zero. $A_1, \ldots, A_n$ and $B_2, \ldots, B_{n-1}$ are unknown functions of the earth parameter and the real number λ. Conventionally, one is only interested in finding the potential at the surface of the earth, so that only the coefficient A_1 needs to be found. The recurrence formulae for A_1 was given by Koefoed (1979) and Parasnis (1986). However, we need the potential at any point in a layered earth. Thus, we have to find all coefficients $A_1, \ldots, A_n$ and $B_2, \ldots, B_{n-1}$. They can be determined by solving the system of $2(n-1)$ linear equations obtained from the continuity conditions of the potential and the normal current density at the layer interfaces $H_j (j = 1, \ldots, n-1)$. The solution is straightforward but tedious. The solutions are:

$$A_1 = \frac{I\rho_1}{2\pi}\mathrm{e}^{-2\lambda h_1}\frac{P_{12}}{1 - P_{12}\mathrm{e}^{-2\lambda h_1}}, \tag{A4}$$

$$A_2 = \frac{I\rho_1}{2\pi}\frac{1 + P_{12}}{1 - P_{12}\mathrm{e}^{-2\lambda h_1}}\frac{1}{1 + P_{23}\mathrm{e}^{-2\lambda h_2}}, \tag{A5}$$

$$B_2 = P_{23}\mathrm{e}^{-2\lambda H_2} A_2, \tag{A6}$$

$$A_n = (1 + P_{n-1,n})A_{n-1}. \tag{A7}$$

$A_3, \ldots, A_{n-1}$ and $B_3, \ldots, B_{n-1}$ are given by

$$A_i = \frac{1 + P_{i-1,i}}{1 + P_{i,i+1}\mathrm{e}^{-2\lambda h_i}} A_{i-1},$$

$$B_i = P_{i,i+1}\mathrm{e}^{-2\lambda H_i} A_i, \quad i = 3, \ldots, n-1, \tag{A8}$$

where

$$P_{i,i+1} = \frac{Z^{(i+1)} - \rho_i}{\rho_i + Z^{(i+1)}},$$

$$Z^{(i)} = \rho_i \frac{Z^{(i+1)} + \rho_i \tan h(\lambda h_i)}{\rho_i + Z^{(i+1)} \tan h(\lambda h_i)},$$

$$Z^{(n)} = \rho_n$$

for $i = 1, \ldots, n-1$.